

X-ray Preionisation Powered by Accretion on the First Black Holes. II: Cosmological Simulations and Observational Signatures

Massimo Ricotti¹, Jeremiah P. Ostriker¹ and Nickolay Y. Gnedin²

¹ *Institute of Astronomy, Madingley Road, Cambridge CB3 0HA, UK*

² *Center for Astrophysics and Space Astronomy, University of Colorado, Campus Box 389, Boulder, CO 80309, USA*
ricotti@ast.cam.ac.uk, jpo@ast.cam.ac.uk, gnedin@casa.colorado.edu

Accepted —. Received —; in original form 10 December 2002

ABSTRACT

We use numerical simulations of a cosmological volume to study the X-ray ionisation and heating of the intergalactic medium by an early population of accreting black holes. By considering theoretical limits on the accretion rate and observational constraints from the X-ray background and faint X-ray source counts, we find that the maximum value of the optical depth to Thompson scattering that can be produced using these models is $\tau_e \simeq 0.17$, in agreement with previous semianalytic results. The redshifted soft X-ray background produced by these early sources is important in producing a fully ionised atomic hydrogen in the low density intergalactic medium before stellar reionisation at redshift $z \sim 6 - 7$. As a result stellar reionisation is characterised by an almost instantaneous “overlap phase” of H II regions. The background also produces a second He II reionisation at about redshift three and maintains the temperature of the intergalactic medium at about 10,000 K even at low redshifts.

If the spectral energy distribution of these sources has a non-negligible high energy power-law component, the luminosity in the soft X-ray band of the “typical” galaxies hosting intermediate-mass accreting black holes is maximum at $z \sim 15$ and is about one or two orders of magnitude below the sensitivity limit of the Chandra deep field. We find that about a thousand of these sources may be present per square arcmin of the sky, producing potentially detectable fluctuations. We also estimate that a few rare objects, not present in our small simulated volume, could be luminous enough to be visible in the Chandra deep field. XEUS and Constellation-X satellites will be able to detect more of these sources that, if radio loud, could be used to study the 21 cm forest in absorption.

A signature of an early X-ray preionisation is the production of secondary CMB anisotropies on small angular scales (< 1 arcmin). We find that in these models the power spectrum of temperature fluctuations increases with decreasing angular scale ($\Delta T \sim 16 \mu\text{K}$ at ~ 1 arcsec scales), while for stellar reionisation scenarios the power decreases on smaller scales. We also show that the redshifted 21 cm radiation from neutral hydrogen can be marginally detected in emission at redshifts $7 < z < 12$. At a redshift of about $z \sim 30$ a stronger and narrower (in redshift space) signal in absorption against the CMB, that is peculiar to these models, could be detectable.

Key words: cosmology: theory – methods: numerical

1 INTRODUCTION

The WMAP satellite measured an optical depth to Thompson scattering of the IGM $\tau_e \simeq 0.17 \pm 0.04$ (Kogut et al. 2003). The result, implies a much earlier start of reionisation with respect to the redshift when reionisation was completed (at $z_{\text{rei}} \sim 6$, as estimated from the absorption spectra of high redshift quasars). This has also been interpreted as one of the stronger pieces of evidence for the importance of zero-metallicity (Population III) stars in the early universe (*e.g.*, Cen 2003a; Wyithe & Loeb 2003; Somerville & Livio 2003; Ciardi et al. 2003; Sokasian et al. 2004; Chiu et al. 2003) and of the formation of the first small

mass galaxies (with $M_{\text{dm}} \sim 10^6 - 10^8 M_{\odot}$), a topic that is still under debate (*e.g.*, Haiman et al. 1997; Ricotti et al. 2001, 2002b; Machacek et al. 2003). In a previous paper (paper I), Ricotti & Ostriker (2004a) have argued that, even assuming the most favorable properties for Population III, it is difficult or impossible to produce the measured value of τ_e using UV radiation from Population III stars. The main problems with this scenario are the negative feedback from ionising radiation, mechanical feedback from SN explosions and the contamination of high density regions by detritus from the same stars which produce the ionising radiation. Taking into account the metal enrichment from SNe

and pair instability SNe the Population III epoch turns out to be so short lived that Population III stars will never be able to complete the reionisation of the IGM. But if a significant fraction of Population III stars, instead of exploding as SNe, implode into black holes (BHs), then the negative feedback on star formation is much reduced and the UV radiation produced by thermonuclear reactions in the first stars might be important for reionisation. In Ricotti & Ostriker (2004b) (paper IIa) we have shown that in such a scenario, the X-ray background produced by accretion onto stellar mass seed black holes would be more effective in producing the large τ_e measured by WMAP than the UV radiation from the parent stars. Madau et al. (2004) have also investigated a scenario in which accretion on intermediate-mass black holes produces the large optical depth to Thomson scattering measured by WMAP. In their paper they focus is on the physics of black hole mergers and accretion onto seed black holes. Their paper is complementary to our studies that, instead, focus on radiative transfer processes. Before the WMAP measurement of a large τ_e , the effect of X-ray preionisation has been investigated by Oh (2001) and Venkatesan et al. (2001). The values of τ_e that they found were smaller since the H I ionisation was produced by secondary photoelectrons that can ionise the gas to a maximum of 10% ionisation fraction. We find larger values of τ_e , consistent with WMAP, because of the additional ionisations produced by the redshifted soft X-ray background.

In this paper we complement the semianalytic results presented in paper IIa by using hydrodynamic cosmological simulations that include a recipe for star formation and 3D radiative transfer for hydrogen and helium ionising radiation. An approximate solution of the radiative transfer equations (Gnedin & Abel 2001) is used to speed up the calculations and make the coupling of the radiative transfer and hydrodynamic equations computationally feasible. In addition, radiative transfer for the optically thin X-ray radiation and H₂ dissociating radiation is solved exactly. Line radiative transfer in the H₂ Lyman-Werner bands ($11.3 < h\nu < 13.6$ eV) is also solved exactly for the volume averaged component of the radiation field. Using this method we are able to simulate local and global radiative feedback effects of galaxy formation on cosmological scales.

The results of the cosmological simulations are used to predict the distinctive observational signatures of the X-ray preionisation scenario compared to stellar reionisation models. We find that, if this scenario is correct, a new population of X-ray sources that do not have optical counterparts may be detected in the Chandra deep field. Interestingly, these sources, that might be high redshift AGNs but also galaxies hosting a large number of bright Ultraluminous X-ray sources (ULXs), might have been already observed (Koekemoer et al. 2003).

Simulations of a cosmological volume allow us to construct maps for the secondary CMB anisotropies produced after recombination by the first sources of ionising radiation. We also use the simulation outputs and the semianalytic models presented in paper IIa to calculate the redshifted 21 cm radiation from the IGM prior to reionisation in emission or absorption against the CMB. In the X-ray preionisation scenario the IGM is only partially ionised at redshift $z > z_{\text{rei}} \simeq 6-7$. Therefore, the 21cm signal from the IGM at $z < 12$ can be detected even though it is rather weak. Note that, in stellar reionisation scenarios that can produce the optical depth to Thomson scattering observed by WMAP, the expected 21cm signal is instead undetectable. Finally we estimate the additional high energy background due to the postulated population of high redshift X-ray sources and its subsequent signatures [(10 ± 5)% in the 2-50 keV bands].

This paper is organised as follows: in § 2 we show the results of cosmological simulations of X-ray preionisation by mass accretion on seed BHs. In § 3 we estimate the number of detectable X-ray point sources at high redshift. In § 4 we calculate the redshifted 21cm signal for one of our simulations in absorption/emission against the CMB. In § 5 we compute the amplitude of the power spectrum of CMB secondary anisotropies on scales of a few arcmin produced by X-ray preionisation and stellar reionisation scenarios. We summarise the results in § 6 and we discuss the observational signatures of the X-ray preionisation scenario when compared to stellar reionisation scenarios.

2 COSMOLOGICAL SIMULATIONS

In this section we show the results of cosmological simulations including radiative feedback effects and feedback from SN explosions. The code has been implemented and used extensively to study the formation of the first galaxies. In this study we have run four new simulations to study the effects of SN explosions and an early X-ray background. The simulations were run on COSMOS, an SGI Origin 38000 in DAMPT at Cambridge University.

We adopt a concordance Λ CDM cosmological model with parameters consistent with the analyses of Spergel et al. (2003) and Tegmark et al. (2004): $\Omega_m = 0.3$, $\Omega_\Lambda = 0.7$, $h = 0.7$ and $\Omega_b = 0.04$. The initial spectrum of perturbations has $\sigma_8 = 0.91$ and $n_s = 1$. The box size is $L_{\text{box}} = 1 \text{ h}^{-1} \text{ Mpc}$ (comoving) and the grid has $N_{\text{box}}^3 = 128^3$ cells. We achieve a maximum mass resolution of $M_{DM} = 3.94 \times 10^4 \text{ h}^{-1} M_\odot$ and spatial resolution of $488 \text{ h}^{-1} \text{ pc}$ (comoving). We fully resolve the star formation in objects within the mass range $5 \times 10^5 M_\odot \lesssim M_{DM} \lesssim 10^9 M_\odot$. All simulations start at $z = 100$ and end at $z \approx 8$. After this redshift we stop the simulations because the simulated volume ceases to be a statistically representative fraction of the universe.

2.1 The Code

The simulations were performed with the ‘‘Softened Lagrangian Hydrodynamics’’ (SLH-P³M) code described in detail in Gnedin (1995). The cosmological simulation evolves collisionless DM particles, gas, ‘‘star-particles’’ and the radiation field in four frequency bands: optically thin radiation, H I, He I and He II ionising radiation. The radiative transfer is treated self-consistently (*i.e.*, coupled with the gas dynamics and star formation) using the OTVET approximation (Gnedin & Abel 2001). Star particles and BHs are formed as per equation (1) in each resolution element that sinks below the spatial resolution of the code. The code adopts a deformable mesh to achieve higher resolution in the dense filaments of the large scale structure. We solve the line radiative transfer in the H₂ Lyman-Werner bands for the background radiation, we include the effect of secondary ionisation of H and He by X-rays, heating by Ly α scattering, detailed H₂ chemistry and cooling, and the absorbed stellar energy distribution (SED) of the sources that depends on the mean UV escape fraction (Ricotti et al. 2002a). Here we also include the effect of SN explosions using the method in Gnedin (1998). In Ricotti et al. (2002a) we discussed extensively the details of the code and the physics included in the simulation, focusing on simulations of the first galaxies. We also performed numerical convergence studies that are especially crucial in this case. High mass resolution is needed because the objects that we want to resolve have masses $10^5 M_\odot \lesssim M_{\text{dm}} \lesssim 10^8 M_\odot$. Moreover, the box size has to be large enough in order to include at least a few

Table 1. Input parameters for hydrodynamic simulations with radiative transfer.

#	RUN	N_{box}	L_{box} h^{-1} Mpc	Mass Res. $h^{-1} M_{\odot}$	Res. h^{-1} pc	g_{ν}	ϵ_*	$\epsilon_{\text{UV}}(f_{\text{esc}})$	ϵ_{qso}	z_{off}	F_{IMF}
1	M-PIS	128	1.0	3.94×10^4	488	Pop III	0.1	2×10^{-3}	2×10^{-3}	8	7
2	M-SN1	128	1.0	3.94×10^4	488	Pop III	0.1	3×10^{-4}	2×10^{-3}	10	1
3	M-SN2	128	1.0	3.94×10^4	488	Pop III	0.1	3×10^{-5}	2×10^{-3}	11	0.1
4	M-BH	128	1.0	3.94×10^4	488	Pop III	0.1	3×10^{-5}	see Eq. 2	13	0.1

Parameter description. *Numerical parameters:* N_{box}^3 is the number of grid cells, L_{box} is the box size in comoving h^{-1} Mpc. *Physical parameters:* g_{ν} is the normalised SED (Population III). The meaning of the other parameters is explained in the text (§ 2.1).

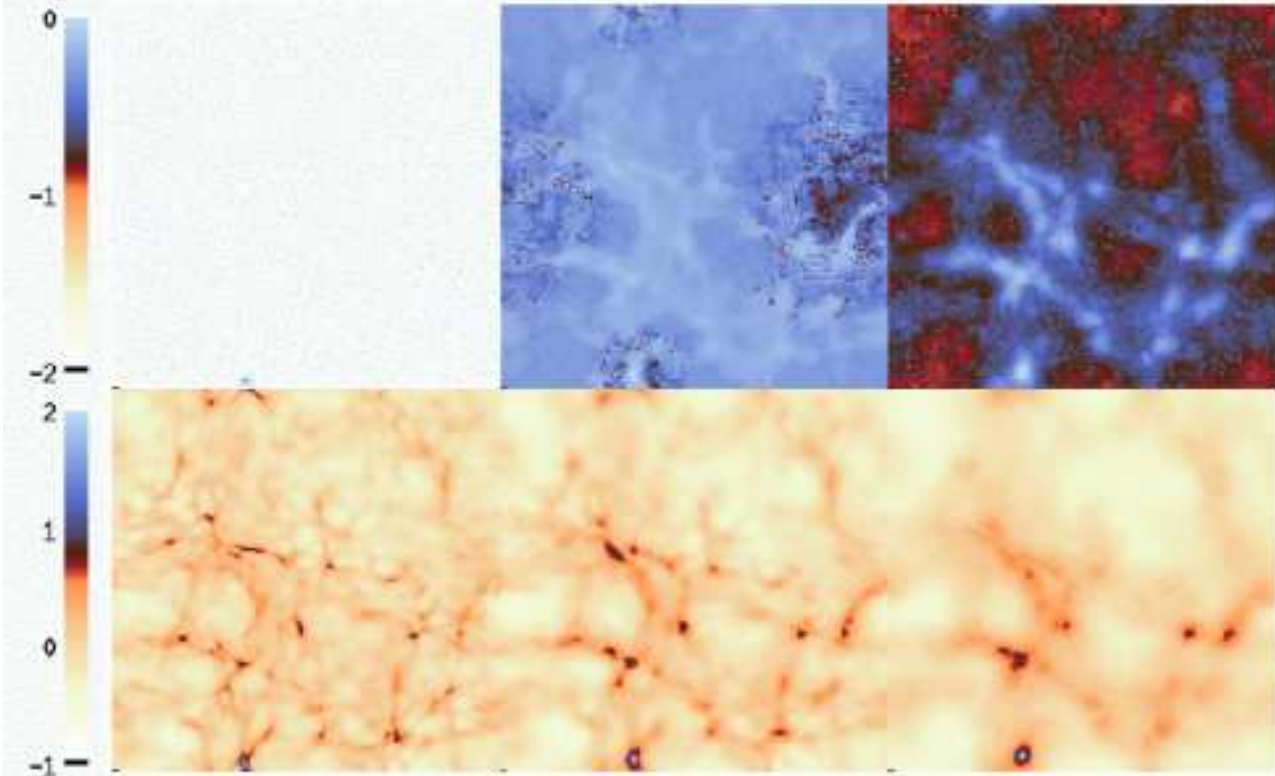


Figure 1. Slices through the volume of the simulation M-BH (*cf.*, table 1) at redshift $z = 19, 12.5$ and 9 from left to right. The top panels show the hydrogen ionisation fraction (in logarithmic scale) and the bottom panels the gas overdensity (in logarithmic scale). Note the ionisation fraction in the voids is larger than in the denser filaments. The overdense gas is smoothed on the filtering scale (*i.e.*, time averaged Jeans length) by the X-ray reheating that precedes the IGM partial preionisation.

of the rare first objects. The first small-mass galaxies will form at $z \sim 30 - 40$ from 3σ or more rare density perturbations; the first normal galaxies with $M_{\text{dm}} \gtrsim 5 \times 10^8 M_{\odot}$ form at $z \gtrsim 15$, also from 3σ perturbations. Below, we summarise the meaning of the free parameters in the simulations.

- ϵ_* : Efficiency of star formation for the adopted star formation law,

$$\frac{d\rho_*}{dt} = \epsilon_* \frac{\rho_{\text{gas}}}{t_*}, \quad (1)$$

where ρ_* and ρ_{gas} are the stellar and gas density, respectively. t_* is the maximum between the dynamical and cooling time.

- ϵ_{UV} : Energy in ionising photons emitted by stars per rest mass energy of H atoms ($m_{\text{H}}c^2$) transformed into stars. This parameter depends on the IMF and stellar metallicity. We use Population III stars SED.

- $\langle f_{\text{esc}} \rangle$: escape fraction of ionising photons from a cell. It is resolution dependent.

- ϵ_{qso} : Energy in ionising photons emitted by quasars per rest mass energy of H atoms ($m_{\text{H}}c^2$) transformed into stars. This means that, if $\epsilon_{\text{qso}} = \text{const}$, the total UV luminosity from quasars is proportional to that from massive stars. We use the template spectrum given in § 3.1 of paper IIa. The spectrum is a double power law with a soft X-ray bump produced by absorption of UV photons by the obscuring torus and the ISM around the BH (in particular the absorption is produced by an H I column density of 10^{19} cm^{-2} and He with ionisation fractions $x_{\text{He I}}/x_{\text{H I}} = 0.1$, $x_{\text{He II}}/x_{\text{H I}} = 0.1$). In paper I we mentioned that our spectrum is similar to the template spectrum derived by Sazonov et al. (2004). This statement is actually misleading since our spectrum is softer, having a cutoff at about 100 eV instead of 1 keV. We will discuss in § 2.3 the importance of soft X-rays and we will quantify how the cutoff energy in the quasar spectrum affects our results. The energy density in the X-ray bands is about $\beta = 20\%$ of the total and 40 % of the energy of H ionising radiation ($\epsilon_{\text{X}} = 0.4\epsilon_{\text{qso}}$, because of the local absorption of UV photons). The accretion rate at the Eddington limit

with efficiency $\epsilon = 0.2$, defined in § 3 of paper IIa, is given by $0.2\beta\dot{\rho}_{\text{ac}} = \epsilon_X\dot{\rho}_*$, where $\dot{\rho}_*$ is the star formation rate and $\dot{\rho}_{\text{ac}}$ is the accretion rate onto BHs.

- z_{off} : redshift at which the X-ray emission by quasars turns off. We assume that $\epsilon_{\text{qso}} = 0$ at $z < z_{\text{off}}$.

- F_{IMF} : This parameter is proportional to the mean metallicity yield and energy input by SN explosions of the stellar population. We have $F_{\text{IMF}} = 1$ for Population II stars with a Salpeter IMF. But Population III stars could have $F_{\text{IMF}} > 1$ if the IMF is top-heavy and pair-instability SNe are dominant. If the IMF is dominated by subluminescent BH forming SNe, or by stars with $M_* > 260 M_{\odot}$ that collapse directly into BHs without exploding as SNe (see § 3 of paper IIa), we have $F_{\text{IMF}} < 1$.

We have run four simulations that differ mainly in the epoch at which the early accretion onto seed BHs takes place (*cf.*, table 1). In paper IIa we have studied three models: an early preionisation model (with preionisation starting at redshift $z_{\text{pre}} \sim 25$), an intermediate preionisation model ($z_{\text{pre}} \sim 20$) and late preionisation model ($z_{\text{pre}} \sim 15$). Due to the limited volume and resolution of our simulations, the first sources form at redshift $z \sim 27$, later than in the semianalytic models that do not suffer of these limitations. The radiation background from the first sources (*cf.*, Fig. 6) builds up to relevant values only about one Hubble time after the formation of the first source, corresponding to a redshift $z \sim 20$. At this redshift the ionisation fraction of the IGM will start increasing. For this reason, using numerical simulations, we cannot simulate the early preionisation model presented in paper IIa. In order to simulate earlier object formation, we would need simulations with comparable mass resolution to the present but of a larger volume of the universe. In such a simulation the first galaxies would have formed at redshift $z \sim 40$ from rare (*i.e.*, 5σ) peaks of the Gaussian perturbations in the density field, allowing the earlier production of seed BHs and preionisation by the X-ray background.

In the first three simulations in table 1 (M-PIS, M-SN1 and M-SN2) we have assumed a step function for the efficiency of X-ray emission ϵ_{qso} (*i.e.*, $\epsilon_{\text{qso}} = 0.002$ at $z > z_{\text{off}}$ and zero afterwards). This means that in the first three simulations we assume that the local black hole accretion rate is proportional to the local SFR and we explore the effects of changing the stellar IMF and $\langle f_{\text{esc}} \rangle$. In the simulation M-PIS the IMF is top-heavy, $\langle f_{\text{esc}} \rangle = 1$ and the energy input from SN explosions is 7 times larger than for a Salpeter IMF. The parameters of this first simulation describe a scenario in which Population III stars are supermassive and a substantial fraction of them explodes as pair-instability supernovae. In the simulation M-SN1 we assume a Salpeter IMF and $\langle f_{\text{esc}} \rangle = 1$. The parameters of this simulation are also consistent with a top-heavy IMF combined with $\langle f_{\text{esc}} \rangle \ll 1$. The simulation M-SN2 is the same as M-SN1 but has $\langle f_{\text{esc}} \rangle = 10\%$ and the effect of SN explosions is 10 times smaller. The parameters of this simulation are also consistent with a mildly top-heavy IMF combined with $\langle f_{\text{esc}} \rangle < 10\%$ and subluminescent or negligible SN explosions. This assumption is justified by the fact that zero-metallicity stars, if more massive than $\sim 260 M_{\odot}$, may collapse directly into BHs without exploding as SN. Another possibility is that the energy of SN explosions in zero-metallicity stars with masses $\lesssim 100 M_{\odot}$, is smaller than the canonical value $E = 10^{51}$ ergs (Umeda & Nomoto 2003).

The fourth simulation (M-BH) is the same as M-SN2 but has larger and time-dependent efficiency of X-ray emission, ϵ_{qso} . The X-ray emissivity is similar to the one used in the semianalytic model M3 (the intermediate preionisation model) of paper IIa and it is physically motivated in § 3 of that paper. The time dependent

function for ϵ_{qso} is given by

$$\epsilon_{\text{qso}} = 0.2 \times \begin{cases} \exp[(39/(1+z))^{1.5}] & \text{if } z > 17 \\ 0.0016((1+z)/15)^{20} & \text{if } z < 17. \end{cases} \quad (2)$$

The efficiency ϵ_{qso} has a maximum at $z = 17$ and then quickly decreases. This is the most interesting simulation because the function ϵ_{qso} is a fit to a realistic model for accretion and because, as shown in the next section, produces a value of the optical depth in agreement with the WMAP measures (*cf.*, § 2.2).

2.2 Results

The soft X-ray and hard UV flux from the first accreting BHs are initially the most efficient in ionising the intergalactic gas in the immediate vicinity of each source. Thus the topology of IGM ionisation is initially characterised by small Strömgren spheres around the most luminous sources. But, due to the long mean free path of X-ray photons, the background produced by distant sources quickly dominates the ionisation rate and the IGM becomes partially ionised almost uniformly. Due to the negligible recombination rate, the voids have a larger fractional ionisation than the denser filaments. The evolution of the topology of preionisation is shown in the top panels of Fig. 1 where we show the neutral fraction of the IGM in a slice through the simulation number four in table 1 at redshift $z = 19, 12.5$ and 9. The bottom panels show the gas overdensity in the same simulation. It is evident from the smooth appearance of the filamentary structure that the X-rays, heating the IGM and increasing the Jeans mass, have smoothed the gas on scales (*i.e.*, the “filtering” scale) larger than the size of the dark matter filaments.

In Fig. 2(left) we show the BH accretion rate (top panel) and the baryon fraction in BHs, ω_{BH} (bottom panel), for the four simulations whose parameters are listed in table 1.

In paper IIa we have discussed the physical requirements needed to produce such accretion histories. Here we do not discuss this matter further but we note that, given the assumed SED of mini-quasars, it is possible to determine an upper limit for the global accretion rate. This limit is determined by the requirement that the early sources of X-rays contribute to less than 10 – 20% of the observed X-ray background in the 2 – 10 keV bands. The sources that constitute the bulk of the soft X-ray background has now been resolved and identified (mainly Seyfert galaxies at $z \sim 1 - 2$). Recently De Luca & Molendi (2004) have estimated that that about 20% of the observed background may be produced by a new population of faint X-ray sources, currently undetected within the sensitivity limits of the deepest X-ray surveys. It does not seem that the faint high redshift optically discoverable sources are abundant enough to contribute much to the background (Hunt et al. 2003). So there is some room for the population of sources that we are postulating to exist at high redshift. The solid line in Fig. 2(left) shows the value of the global accretion rate as a function of redshift that would produce the 20% of the X-ray background at $z = 0$ that it is still unaccounted for by lower redshift AGNs.

In Fig. 2(right) we show the star formation rate (top panel) and the baryon fraction in stars, ω_* (bottom panel), for the models in table 1. Depending on the simulation parameters, the thermal feedback on the IGM or internal feedbacks from galactic winds due to photoevaporation and mechanical energy from SN explosions, are dominant in reducing the global star formation rate in small-mass galaxies (Ostriker & Gnedin 1996; Ricotti et al. 2002b).

The results of the simulations confirm the results found using

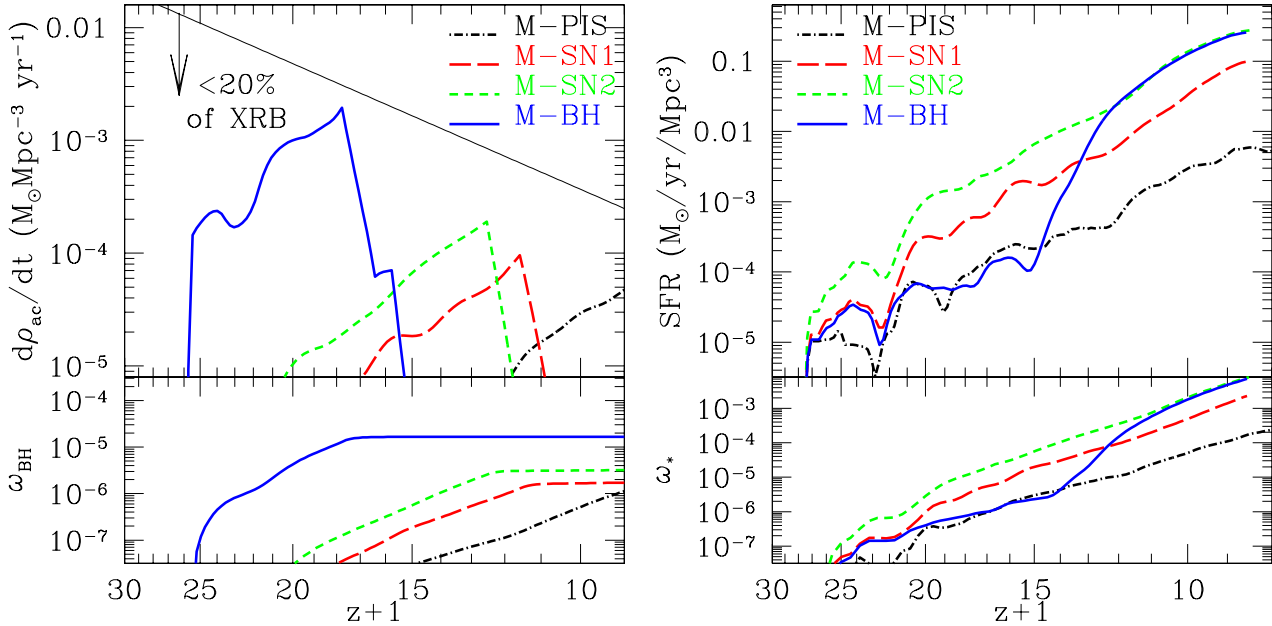


Figure 2. (left) Black hole accretion history for the four models in table 1. (right) Star formation history for the four models in table 1. The simulations differ in the efficiency of X-ray emission (duty cycle), IMF and $\langle f_{\text{esc}} \rangle$. The solid line shows the upper limit of the accretion rate for the SED we have adopted. If the global accretion rate on seed BHs is below the solid line, their contribution to the observed X-ray background at $z = 0$ (at about 10 keV) is less than 20%.

the semianalytic models presented in paper Ia. The main signatures of X-ray preionisation are illustrated in Fig. 3 that plot the hydrogen ionisation history (top panel) and thermal history of the IGM (bottom panel) as a function of redshift for the four simulations in table 1. The early reheating of the IGM to a temperature $T \approx 10^4$ K is reached when the hydrogen ionisation fraction becomes larger than 10% (*cf.*, Figs. 3). This happens because the ionisation rate from energetic secondary photoelectrons becomes inefficient when the fractional ionisation is larger than 10%, consequently most of the energy of the X-ray photons is deposited into heat. If the X-ray background is large enough, the soft X-ray photons emitted from distant sources and redshifted into softer UV photons, can reionise the voids above the 10% fractional ionisation.

The IGM optical depth to electron Thompson scattering, τ_e , and the visibility function,

$$g(z) = \exp(-\tau_e) \frac{d\tau_e}{d\eta}, \quad (3)$$

where η is the conformal time, are plotted in Fig. 4 for the simulations in table 1. We find that, for the most extreme model (run number four in table 1), X-ray preionisation can produce an optical depth to Thompson scattering $\tau_e = 0.17$, in agreement with WMAP measurement. The shape of the visibility function determines the power spectrum at large angular scales of the polarised CMB radiation (EE) and the temperature-polarisation cross correlation (TE). In particular the EE power spectrum can be used to distinguish between models with the same τ_e but different ionisation history because its shape is determined by the redshift at which the visibility function has a peak (Holder et al. 2003). As was found in paper Ia the intermediate preionisation scenario is the most efficient in producing a larger optical depth to Thompson scattering because it is the earlier preionisation scenario that requires the minimum number of ionising photons per baryon (*i.e.*, the recombinations are negligible).

Contrary to the double reionisation models proposed by Cen

(2003b), in the X-ray preionisation models hydrogen is fully reionised only once at low redshift (*e.g.*, by Population II stars at $z \sim 6 - 7$). But in most X-ray preionisation models He II is reionised twice. The helium is doubly ionised a first time at high redshift. Afterward, in most simulations, due to the fast decline in accretion rate onto seed BHs, it partially recombines before redshift nine. But the rate of He III recombination is slow because of the photoionisations from the redshifted X-ray background photons. This is shown in Fig. 5, where we plot the He ionisation history as a function of redshift for the four simulations in table 1. In most simulations He II becomes about fully ionised (60-80% fractional ionisation) before H I reionisation. It is possible to reionise He II before fully reionising H I in the voids if it is the background that dominates the ionisation rate (note that the background spectrum has almost no UV photons). Indeed the soft UV photons cannot ionise the voids because they are absorbed locally while harder photons can still ionise H I but less efficiently than He II.

At redshifts $z \lesssim 9$, due to the redshifted X-ray background, the ionisation fraction of He III starts increasing again and He II becomes roughly fully ionised a second time at $z \sim 3$ (see paper Ia for a discussion on this effect). The temperature of the IGM, due to He II ionisation, remains almost constant from redshift 6 to redshift 3 at about 10,000 K (*cf.*, paper Ia), in agreement with observation of the line widths of the Lyman- α forest (Ricotti et al. 2000).

In Fig. 6 is shown the background radiation at $z = 11.5, 7.8$ and the extrapolated value at $z = 0$ for model M-BH. The observed X-ray background radiation at $z = 0$ is shown with a thick solid line. Even though early accretion on seed black holes produces only 10% of the observed X-ray background (in the 2-10 keV band), at redshift $z \sim 3$ they may have been predominant, indeed most of the X-ray background is produced by Seyfert galaxies at $z \sim 1$. Our analysis of the model constraints posed by the observed unresolved component of the X-ray background (presented in paper Ia and also shown here in Fig. 6) are consistent with the findings of

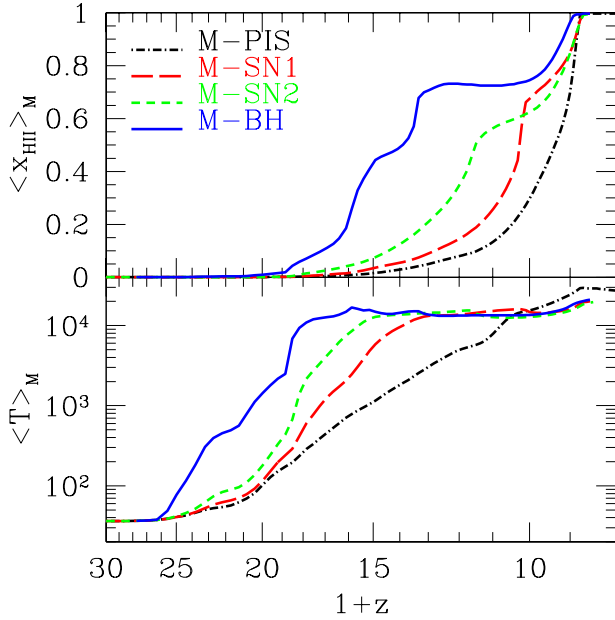


Figure 3. Hydrogen ionisation history (top panel) and thermal history (bottom panel) for the four models in table 1. In models of reionisation by Population III stars hydrogen has usually two distinct epochs of reionisation, the first at redshift $z \sim 17 - 10$ and the second at $z \sim 6 - 7$. In the X-ray preionisation models hydrogen is partially reionised at early times but it is fully reionised only once at low redshift (*i.e.*, by Population II stars at $z \sim 6 - 7$). Note that the reheating of the gas always precedes the reionisation. This characteristic is in common with all the reionisation scenarios.

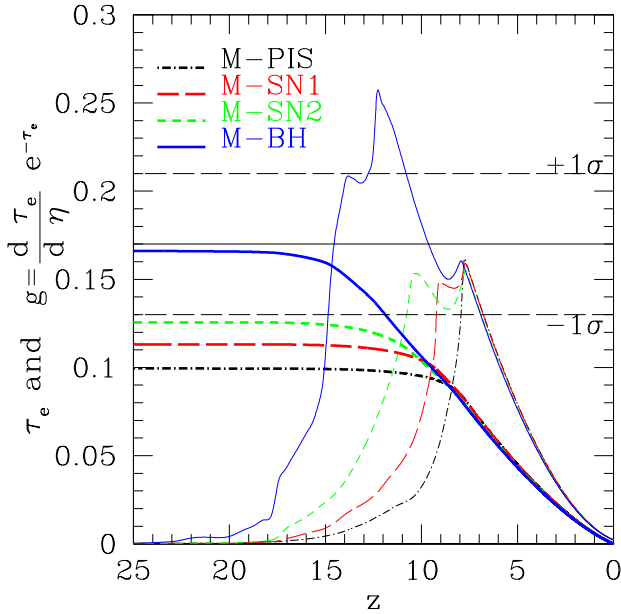


Figure 4. Thomson scattering optical depth, τ_e , and visibility function, $g(z)$, as a function of redshift for the simulations in table 1. A simulation without X-ray preionisation with stellar reionisation by Population II stars at $z \approx 7$ would have $\tau_e = 0.6$.

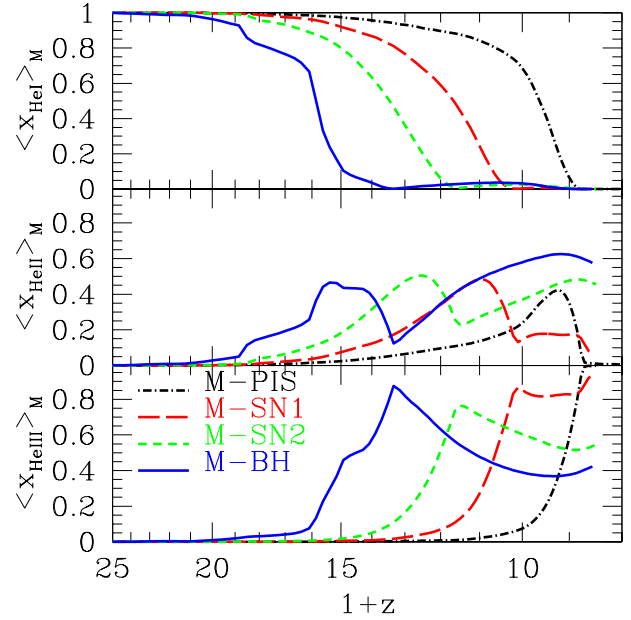


Figure 5. Helium ionisation history for the four models in table 1. In most X-ray preionisation models He II is reionised twice. The helium is doubly ionised a first time at high redshift. Afterwards it partially recombines before redshift 8-9. At redshifts $z \lesssim 8 - 9$, due to the redshifted X-ray background, the ionisation fraction of He III starts increasing again and He II become fully ionised a second time at $z \sim 3$ (see paper IIa for a discussion on this effect). This has also the effect of keeping the temperature of the IGM at about 10,000 K from redshift 6 to 3.

(Dijkstra et al. 2004). They also do not rule out a high redshift mini-quasar population that could partially reionise the IGM to 50% ionisation fraction. In particular, in the case that the quasar spectrum has only a soft X-ray component (*e.g.*, produced by the hot multi-colour accretion disk) and no hard X-ray emission, the X-ray background does not pose any constraint on the number density and luminosity of a putative high redshift population of X-ray sources. Sources with this SED could preionise the IGM very efficiently.

The efficiency of secondary ionisation from energetic photoelectrons is large when the ionisation fraction of the IGM is less than 10%. This is illustrated in Fig. 7 that shows the mass-weighted distribution of the mean hydrogen ionisation, x_{HII} , versus the overdensity for the M-BH simulation at redshift $z \approx 15$ (figure on the left) and 10 (figure on the right). At redshift $z \sim 15$ the hydrogen in most of the IGM volume has a fractional ionisation of 10% or less as expected. Interestingly, at $z \approx 10$, even if reionisation by stellar sources is not complete, the underdense regions are already almost fully ionised. This is due to the intense background in the UV bands arising from the redshifted X-rays emitted by distant sources that ionises the IGM, preferentially in the low density regions that occupy most of the volume. The ionisation fraction in the voids remains large because the recombination time is longer than the Hubble time in these underdense regions. Because the atomic hydrogen in the low density intergalactic medium is almost fully ionised before stellar reionisation at redshift $z \sim 6 - 7$, it follows that stellar reionisation is characterised by an almost instantaneous “overlap phase” of H II regions.

In the remaining paragraphs of this section we describe the results of each simulation in greater detail.

In the simulation M-PIS (dot dashed line), the IMF is top-

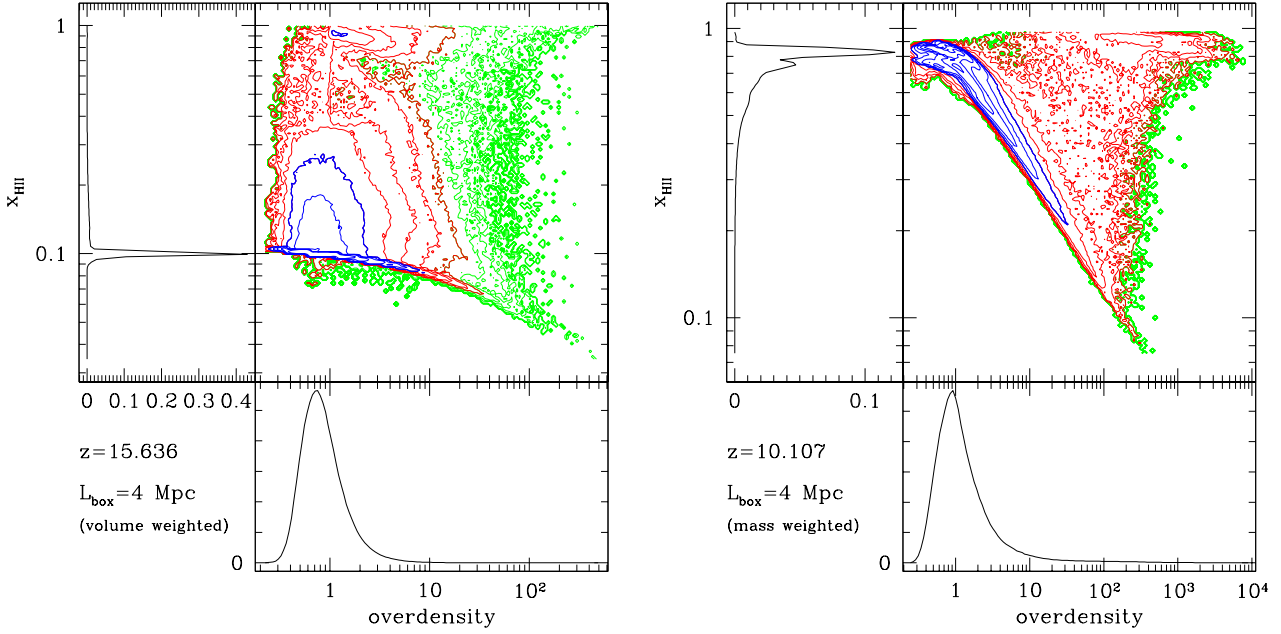


Figure 7. Mass-weighted distribution of the mean hydrogen ionisation fraction versus the overdensity for the M-BH simulation at $z \simeq 15$ (left) and $z \simeq 10$ (right). The stellar sources did not reionise the IGM at this redshift but the underdense regions are already almost fully reionised. UV photons from the redshifted X-ray background ionise the IGM, preferentially the low density regions. The voids remain ionised because the recombination time is longer than the Hubble time.

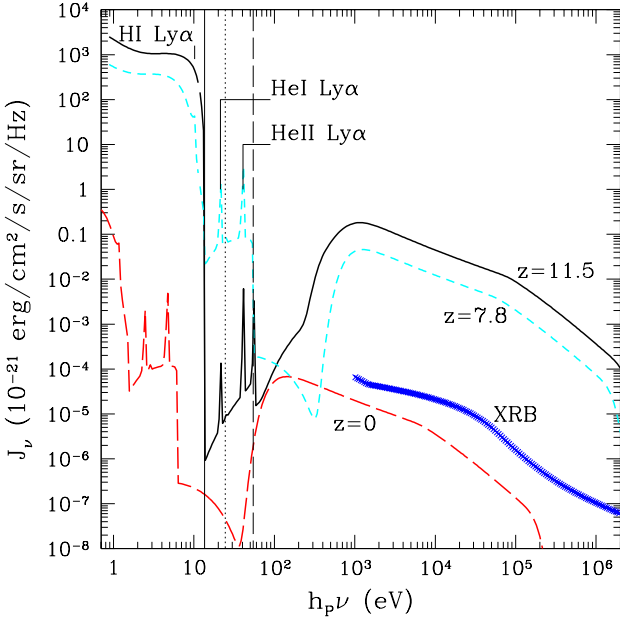


Figure 6. Background radiation at $z = 11.5, 7.8$ and the extrapolated value at $z = 0$ for model M-BH. To guide the eye, the thin vertical lines show the energy of the Lyman continuum of H I, He I and He II. The labels show the Lyman- α lines of H I, He I and He II. The observed X-ray background radiation at $z = 0$ is shown with a thick solid line. Even though early accretion on seed black holes produce only 10% of the observed X-ray background (in the 2-10 keV band), at redshift $z \sim 3$ they may have been predominant, indeed most of the X-ray background is produced by Seyfert galaxies at $z \sim 1$.

heavy, $\langle f_{\text{esc}} \rangle = 1$ and the energy input from SN explosions is 7 times larger than for a Salpeter IMF. This case is one in which pair-instability SNe are important in polluting the IGM and in producing strong mechanical feedback in the ISM. The star formation is strongly suppressed by the SN explosions. At $z \approx 7$ the SFR is $5 \times 10^{-3} M_{\odot} \text{ Mpc}^{-3} \text{ s}^{-1}$, 20 times smaller than the observed value at $z \sim 4 - 6$. The box size of $1 h^{-1} \text{ Mpc}$ is too small to achieve convergence at $z \lesssim 12$ (this is demonstrated more quantitatively in paper I), therefore at those redshifts the star formation is probably underestimated. But the result shows that star formation is strongly suppressed in galaxies less massive than $10^9 M_{\odot}$ for this choice of the IMF. Metal pollution from SN explosions may suppress the formation of Population III stars before $z = 10$, when we stop our simulation. This would reduce the UV emissivity, ϵ_{UV} , and the SN energy output, F_{IMF} . Here, we did not take into account this effect. In this simulation the assumed efficiency of X-ray emission, $\epsilon_{\text{qso}} = 2 \times 10^{-3}$, is too small to have a substantial effect on the ionisation and re-heating of the IGM. Reionisation of H I and He II happens at $z \approx 8$ and the gas is heated to $T \approx 3 \times 10^4 \text{ K}$.

In the simulation M-SN1 (dashed line), we assume a Salpeter IMF and $\langle f_{\text{esc}} \rangle = 1$. Here the global SFR is about 10 times larger than in the M-PIS simulation, because of the less violent feedback from SN explosions. The increased SFR produces a larger X-ray emission that at $z \simeq 12$ re-heats the IGM to $T \simeq 10^4 \text{ K}$ and partially ionises the IGM ($\langle x_e \rangle \simeq 10\%$). The X-ray emission continues to increase until redshift $z = 10$ as a result of the increasing star formation and the electron fraction reaches $\langle x_e \rangle \sim 50\%$. At $z \sim 9$ He II is reionised. In this model after $z_{\text{off}} = 10$ we assume zero X-ray emissivity ($\epsilon_{\text{qso}} = 0$). The He II starts recombining but the ionisation fraction continues to increase, but more slowly. This effect is due to UV photons arising from redshifted X-rays of the background radiation. For this model $\tau_e \sim 0.11$ and the visibility function peaks between redshifts $6 < z < 9$.

The simulation M-SN2 (short dashed line) is the same as M-

Table 2. Results of the hydrodynamic simulations with radiative transfer.

RUN	τ_e	z_g^{max}	y -par $\times 10^{-7}$	ω_{BH} $\times 10^{-5}$	f_{XRB} (%)	$\Gamma(\text{He II})t_H$ (%)
M-PIS	0.10	8	3.0	0.1	19 (12)	> 200
M-SN1	0.11	9	3.1	0.2	11 (6)	60
M-SN2	0.13	10.5	3.3	0.3	9 (5)	25
M-BH	0.17	12	4.4	2.0	17 (8)	20

Meaning of the values in each column: τ_e is the Thomson scattering optical depth; z_g^{max} is the high-redshift maximum of the visibility function $g(z)$ (it also roughly coincides with the redshift of early reionisation of He II); y is the Compton distortion parameter; ω_{BH} is mass fraction in BH in units of the baryon cosmic density at redshift $z = 8$ (to translate ω_{BH} to cosmic BH mass density, ρ_{BH} , multiply by $5.5 \times 10^9 M_\odot \text{Mpc}^{-3}$); f_{XRB} is the fraction of the X-ray background at 50-100 keV (and 2-10 keV, in parenthesis) due to early black holes; $\Gamma(\text{He II})t_H \sim (t_H/n_{\text{He II}})dn_{\text{He II}}/dt$ is the fractional rate of He II photoionisation per Hubble time per helium atom at redshift $z \sim 2 - 3$ due to the redshifted X-ray background.

SN1 but has $\langle f_{esc} \rangle = 10\%$ and the effect of SN explosions is 10 times smaller. This assumption is justified by the fact that zero-metallicity stars may collapse directly into BHs without exploding as SN. Another possibility is that the energy of SN explosions in zero-metallicity stars is smaller than the canonical value $E = 10^{51}$ ergs (Umeda & Nomoto 2003). The results for this simulation are analogous to M-SN1 but by virtue of the larger SFR (by three times), partial X-ray ionisation and re-heating starts earlier (at $z \sim 14$) and $\tau_e \sim 0.13$.

Finally, simulation M-BH (solid line) is the same as M-SN2 but has a larger X-ray emissivity, ϵ_{qso} . Contrary to previous models where we have assumed a constant value of ϵ_{qso} , here the emissivity is a fit to the semianalytic intermediate preionisation model (model M3 in paper IIa). In this simulation the thermal feedback produced by the X-ray background on the SFR is evident. At $z > 15$ the global SFR is reduced by about one order of magnitude. It starts increasing again and reaches the same magnitude as in the M-SN2 simulation at $z = 12$ when more massive galaxies start to be numerous. The X-ray sources are in the most massive galaxies in which the star formation rate (and the accretion rate) is not suppressed by feedback processes. This can be seen also in the bottom panels of Fig. 1. The X-ray background re-heats and partially ionises the IGM starting at redshift $z \sim 20$. At $z \sim 13$ He II is almost completely reionised and $\langle x_e \rangle \sim 0.7$. Afterwards, He II slowly recombines but H I remains partially ionised until $z = 7$, when reionisation by stellar sources is completed.

In table 2 we summarise the values of some relevant quantities computed from the simulations in table 1. The meaning of the quantities shown in each column of the table are given in the footnote.

2.3 Dependence on the assumed mini-quasars spectra

We have seen that in our models an important contribution to H I and He II reionisation is produced by redshifted soft X-rays. Therefore if the quasar spectrum is strongly absorbed we expect that the importance of X-rays for the H I preionisation and He II double reionisation may be reduced.

Our template spectrum has a cutoff at photon energies of a few 100 eV and therefore differs from Sazonov et al. (2004) absorbed spectrum that does not have emission below few keV. We have assumed that the mini-quasar spectrum is absorbed by a column density of H and He with neutral hydrogen column density $N_{ab} \simeq 10^{19} \text{cm}^{-2}$ (see § 2.1), substantially smaller than in

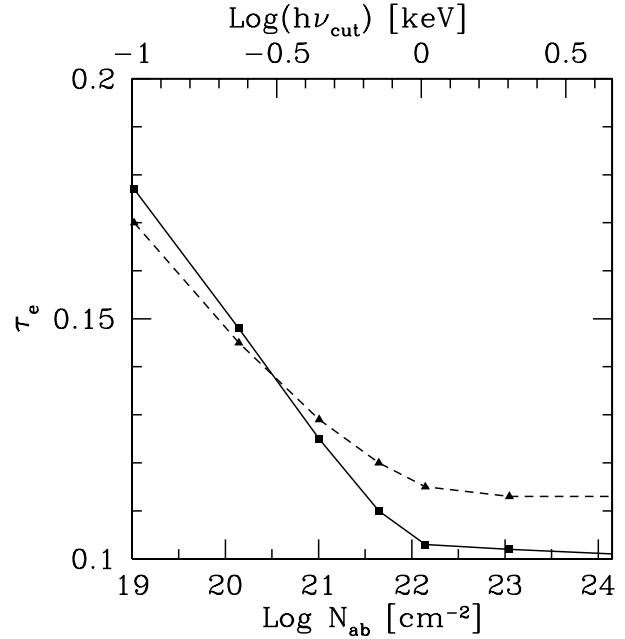


Figure 8. Dependence of the optical depth to Thompson scattering of the IGM, τ_e , on the average absorbed mini-quasar spectrum. We show τ_e as a function of the column density of neutral hydrogen absorbing the quasar spectrum or, equivalently, the cutoff energy of UV and soft X-ray photons in the spectrum (shown on the top axis) for model M4 in paper IIa assuming Population III star SED (dashed line) or Population II star SED (solid line). The results (shown by the points) are calculated using a semianalytic model (see paper IIa) that is equivalent to run M-BH in table 1.

Sazonov et al. (2004). There is no strong theoretical argument in favour of high redshift quasars being strongly absorbed and having no soft X-ray emission. On the contrary, high redshift galaxies have gas components with radii of a few 100 pc and mean gas densities of $10 - 100 \text{cm}^{-3}$. The hydrogen column density is therefore only $N_{ab} \sim (x_{H I}/0.001)10^{19} \text{cm}^{-2}$, where $x_{H I}$ is the hydrogen neutral fraction. Most important, the metallicity is expected to be sub-solar ($Z \sim 0.01 Z_\odot$) and in highly absorbed quasars most of the X-ray absorption is produced by metal lines. The Sazonov et al. (2004) template is therefore more appropriate for quasars at redshifts $z \lesssim 5$, hosted by quite massive galaxies.

More quantitatively, our assumption can be justified by the following arguments. In our simulations the spatial resolution is about $r = 50$ pc therefore, for the assumed column density $N_{ab} = n_{H I}r$, we have $n_{H I} = nx_{H I} \sim 0.1 \text{cm}^{-3}$, where n is the gas density and $x_{H I}$ is the hydrogen neutral fraction. For a gas in photoionisation equilibrium we have

$$x_{H I} = (3 \times 10^{-4} \text{cm}^{-3}) \left(\frac{n}{10 \text{cm}^{-3}} \right) \left(\frac{R}{50 \text{pc}} \right)^2 \left(\frac{S_0}{10^{51} \text{s}^{-1}} \right)^{-1}, \quad (4)$$

where S_0 is the number of ionising photons emitted per second and R is the distance from the source. For example, a $10^4 M_\odot$ black hole accreting at the Eddington limit would emit about $S_0 \sim 10^{50} - 10^{51} \text{s}^{-1}$ EUV photons. Given our choice of the absorbed spectrum we infer a density profile inside our resolution element $n = (60 \text{cm}^{-3})(50 \text{pc}/R)(S_0/10^{51} \text{s}^{-1})^{1/2}$, that seems a quite reasonable assumption.

Nevertheless, it is interesting to study how our results would change if the spectrum has a cutoff at energies $h\nu_{cut} > 100$ eV. We have run a set of semianalytic models assuming that the X-ray

sources are absorbed by larger HI column densities ranging from $N_{\text{ab}} = 10^{19} \text{ cm}^{-2}$ to 10^{25} cm^{-2} (approximately we have $h\nu_{\text{cut}} \sim 100 \text{ eV} (N_{\text{ab}}/10^{19} \text{ cm}^{-2})^{1/3}$). We found that τ_e decreases linearly with increasing $\log N_{\text{ab}}$ and reaches an asymptotic minimum value of $\tau_e \sim 0.1$ for $N > 10^{22} \text{ cm}^{-2}$. In Fig. 8 we show the dependence of the optical depth to Thompson scattering of the IGM, τ_e , on the average absorbed mini-quasar spectrum. We can fit the result shown by the solid line with the function

$$\tau_e = \text{Min}[0.177 - 0.026(\log N_{\text{ab}} - 19), 0.1]. \quad (5)$$

The reionisation of He II at $z \sim 13$ shown in Fig. 5, is also produced by soft X-ray photons emitted by mini-quasars. Increasing the absorbing column density of the quasar spectrum produces a high redshift reionisation only in the low density regions and a partial ionisation in the overdense regions of the IGM. When the column density is $N_{\text{ab}} > 10^{21} - 10^{22} \text{ cm}^{-2}$, the high-redshift reionisation does not happen at all. Similarly, the importance of redshifted X-rays for the low redshift reionisation decreases and is slightly delayed to redshifts $z \sim 2 - 3$ when the absorbing column density increases. Nevertheless, even for large column densities ($N_{\text{ab}} \sim 10^{24} \text{ cm}^{-2}$), redshifted X-rays are still able to reionise He II in underdense regions at $z \sim 2$ and partially ionise the overdense regions. Though, if we assume a Population III SED for the stars and H I reionisation at $z \sim 6.5$, then He II reionisation is dominated by the stars and happens earlier, at $z \sim 3 - 4$. Note that we do not include the contribution from observed AGNs at redshifts $z \lesssim 5$. Perhaps these AGNs are sufficient to produce He II reionisation and IGM reheating at $z \sim 3$ without the need for additional contributions.

Finally, as mentioned earlier, it is plausible that the spectra of high redshift X-ray sources have only a soft X-ray component produced by thermal emission from a multicolour accretion disk and no hard X-ray emission. Accreting intermediate mass black holes, because the disk is hotter than in supermassive black holes, emit in the FUV and soft X-rays. This would be the most favourable scenario for achieving large values of τ_e since soft X-rays efficiently pre-ionise the IGM but high redshift sources, even if very numerous, would be invisible in X-ray and optical deep fields and would not contribute to the observed X-ray background.

3 NUMBER COUNTS OF POINT SOURCES IN THE X-RAY BANDS

We have shown that the high redshift X-ray sources (that we postulate to produced the observed τ_e of the IGM) produce less than 20% of the observed X-ray background. In this section we calculate their contribution to the luminosity function of X-ray point sources. Available Chandra deep field observations can already constrain the most extreme models (paper Iia, Dijkstra et al. 2004) and the future observations with Constellation-X (White & Tananbaum 1999) and XEUS will be a factor ~ 10 times fainter than the current deep survey limit.

It is important to notice that in these calculations we assume a spectral energy distribution of the sources that has a non-negligible high energy power-law component (*cf.*, Fig. 4 in paper Iia), in agreement with observations of QSOs and ULX in the local universe. But if the source spectra are dominated by a multicolour disk thermal component their contribution to both the X-ray background in the 2-50 keV bands and the faint source counts would be negligible. Instead the full ionisation of atomic hydrogen in the low density IGM before redshift $z \sim 7$, the He II reionisation at

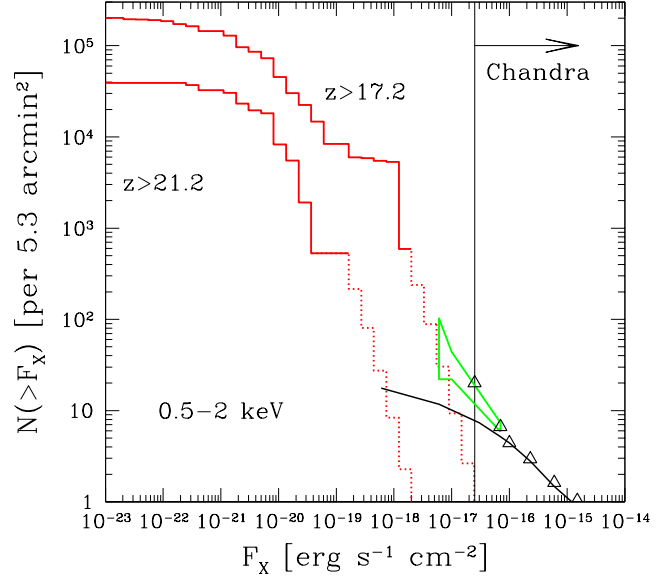


Figure 9. Number counts of X-ray sources in the 0.5-2 keV band for the M-BH run (solid histogram). The brighter tail of the luminosity function is produced by the most massive galaxies at redshift $z \sim 17$ hosting either a supermassive BH of about $10^5 M_{\odot}$ accreting at near the Eddington rate or several intermediate-mass BHs with the same total mass. The dashed portion of the histogram is an extrapolation based on the Press-Schechter formalism. The thin vertical line shows the sensitivity limit of $F_X = 2.5 \times 10^{-17} \text{ erg s}^{-1} \text{ cm}^{-2}$, of the 2 Ms Chandra deep field in the 0.5-2 keV band, the triangles show the number counts of point sources and the solid line a model prediction for the expected counts from AGNs. Finally the closed polygon shows the expected steepening of the counts based on the statistics of pixel fluctuation from unresolved point sources. The observed steepening of the number counts slope at fluxes $F_X \lesssim 10^{-16}$ is consistent with the predictions of our simulation but it is also the predicted contribution of starburst galaxies. The high- z sources, contrary to starburst galaxies, do not have optical counterparts but could be detectable in the infrared if they are not obscured locally by dust.

$z \sim 3$ and reheating of the low-redshift IGM is produced by the redshifted X-ray background independently of the assumed spectra of these early sources.

In our models we do not make assumptions about the mass function of BHs in each galaxy, but only on their total mass and accretion efficiency. Two scenarios are therefore plausible for the X-ray emission. If seed BHs quickly merge into a massive BH at the centre of galaxies through dynamical friction, the X-ray sources will look like small AGNs (mini-quasars). If the seed BHs do not merge efficiently, in each galaxy we could have several off-centre X-ray sources produced by accreting intermediate mass BHs orbiting the galaxy. These sources would be similar to ULXs observed in nearby galaxies, but more numerous (tens or hundreds per galaxy) or more luminous. This new type of X-ray sources could be common in the early universe if primordial galaxies are compact and gas rich. This is expected in young galaxies with masses $M_{\text{dm}} \gtrsim 10^8 M_{\odot}$ in which stellar winds did not evaporate all their gas (Whalen et al. 2003; Ricotti et al. 2004) and star formation did not have time to consume most of the gas. Moreover, in the preionisation models, the number density of intermediate mass BHs was larger in primordial galaxies than in today's galaxies as was shown in Fig. 3 of paper Iia.

The luminosity of accreting BHs in each host galaxy is, by assumption, proportional to the star formation rate in that galaxy, that is, to the ability of the gas in that galaxy to cool efficiently and be accreted toward the centre. Due to the early reheating by the X-ray background and feedback processes (*i.e.*, galactic winds produced by photoionisation and SN explosions) the star formation in the smaller mass galaxies is strongly suppressed and so is the accretion rate on intermediate mass BHs. Moderately larger galaxies are able to retain their gas but they cool so inefficiently that few or no stars at all are formed. When seed BHs are accreted on these galaxies they find a large reservoir of gas and they can start accreting efficiently.

The X-ray luminosity function, shown in Fig. 9, is dominated by the most massive galaxies that are less affected by feedback effects and can retain gas more effectively. This means that the most rare and massive galaxies at $z \sim 15$ are expected to be the most luminous X-ray sources. The volume of our simulation ($1 \text{ h}^{-1} \text{ Mpc}^3$) is large enough to be a representative region of the universe at $z \sim 15$ but it is too small to contain any of these rarer objects. We find that the luminosity of the typical X-ray sources at $z \sim 15$ is two orders of magnitude fainter than Chandra deep field 3σ detection limit for 1.945×10^6 seconds integration time (Alexander et al. 2003) (limiting flux of $2.5 \times 10^{-17} (1.4 \times 10^{-16}) \text{ erg s}^{-1} \text{ cm}^{-2} \text{ sr}^{-1}$ in the $0.5\text{--}2(2\text{--}8) \text{ keV}$ band). But we expect a few thousands of these sources per arcmin². We then use the Press-Schechter formalism to extrapolate the number counts found in our simulation to larger volumes. The extrapolated high luminosity tail of the number counts is shown in Fig. 9 with a dotted line. The plot shows that it is plausible to find a few sources per arcmin² above the detection limit (shown by the vertical line) of the Chandra X-ray deep field (unless the high tail of the luminosity function has a sharper cutoff than in the semianalytic predictions). The triangles show the number counts of point sources of the 2 Ms Chandra deep field in the $0.5\text{--}2 \text{ keV}$ band and the closed polygon shows the expected slope of the luminosity function based on the statistics of pixel fluctuation from unresolved point sources Miyaji & Griffiths (2002). The solid line that fits the number counts is a model prediction for the expected counts from AGNs (*e.g.*, Comastri et al. 1995). We see that the observed steepening of the number counts slope at fluxes $F_X \lesssim 10^{-16}$ is consistent with the predictions of our simulation but it is also consistent with the predicted X-ray contribution by starburst galaxies (*e.g.*, Ptak et al. 2001; Ranalli et al. 2003). In principle it is possible to separate the contribution of these two populations since the high- z sources, contrary to starburst galaxies, do not have optical counterparts but may be detectable in the infrared if they are not obscured locally by dust. The planned spatial resolution of Constellation-X and XEUS of about 5 arcsec is not sufficient to avoid source confusion (Mushotzky, private communication). The cross correlation of the unresolved X-ray background fluctuation with the optical number counts may be used to separate the contribution of the high redshift population from the starburst population.

This prediction has exciting consequences for the direct observability of X-ray sources at redshifts as high as $z \sim 15$. Interestingly, Koekemoer et al. (2003) describe a possible new class of X-ray sources that have robust detections in ultra-deep Chandra data, yet have no optical counterpart in deep multi-band GOODS Hubble Space Telescope (HST) ACS images. Their ratios of X-ray to optical fluxes are at least an order of magnitude above those generally found for other AGN, even those that are harboured by reddened hosts. The authors conclude that if these sources lie above redshifts 6-7, such that even their Lyman- α emission is redshifted out of the bandpass of the ACS $z(850)$ filter, then their optical and

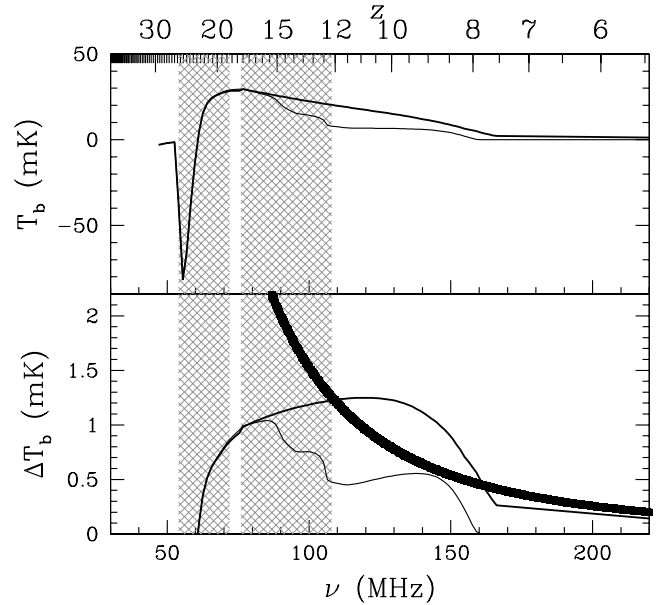


Figure 10. Top panel: the mean redshifted 21 cm signal as a function of frequency and redshift for the simulation run M-BH (thin lines) and our fiducial semi-analytical model (thick lines). The two hatched zones show the locations of TV and FM radio bands within which is likely that no observations will be possible due to man-made interference. Bottom panel: the fluctuations in the redshifted 21 cm signal in a beam of $10'$ and 1 MHz bandwidth. The solid black band is the sensitivity limit of a filled dish aperture telescope for 1000 hours of integration.

X-ray fluxes can be accounted for. They find seven of these sources in the field, in agreement with our estimates for the M-BH run. In our model, if the source emission extends to the rest frame visible/UV bands (*i.e.*, if they are not heavily reddened by dust), they should be detectable in the infrared above $2\text{--}3 \text{ micron}$. Otherwise they should be visible only in X-ray bands and in the FIR at about $100 \mu\text{m}$.

The postulated existence of this mini-quasar population increases the probability of finding a few radio loud sources at $z \sim 17$, that could be successfully used to study the redshifted 21 cm absorption lines produced by the hyperfine transition of neutral hydrogen in the IGM before reionisation (Carilli et al. 2002). Next we discuss further the radio signal at $21(z+1) \text{ cm}$.

4 REDSHIFTED 21 CM LINE IN EMISSION AND ABSORPTION

One possible observational test for our model is the detection of redshifted 21 cm radiation from high redshift (Madau, Meiksin, & Rees 1997; Tozzi et al. 2000). Fig. 10 shows the predicted mean and rms signal for our representative simulation and the best-fit fiducial model. The only instrument capable of detecting the redshifted 21 cm signal is the projected Low Frequency Array (LOFAR). The solid black band shows the expected LOFAR sensitivity for observations with the core (2 km in diameter) for 1000 hour integration time.

In calculating the expected 21 cm signal, we included three physical effects that influence the level population for the hyperfine transition in hydrogen atom: pumping by Lyman- α photons

and collisions with electrons and neutral atoms (Tozzi et al. 2000). The former is the dominant effect at lower redshifts ($z < 20$), while the latter is important at higher redshifts. We then simulated a number of lines of sight through the computational box and averaged over them to properly include the effect of velocity focusing: because most of the emission comes from the high density regions, which are collapsing, velocity focusing increases the effect by a small but not negligible factor.

Fluctuations in the expected 21 cm signal, however, come from large spatial scales (larger than about 10 Mpc). The density fluctuations in this regime are linear, and can be computed analytically (Gnedin & Shaver 2004).

As one can see from Fig. 10, the mean signal is well within the sensitivity of existing or proposed low frequency radio telescopes (such as Arecibo, LOFAR, or SKA). However, the main challenge to observing the mean signal is not the sensitivity, but rather the foreground contamination from the Galaxy (*cf.*, Oh & Mack 2003). The smoothly variable emission signal will most likely be unobservable, but in our model a remarkable opportunity arises: a sharp absorption feature at $z \sim 25$ falls just outside the broadcast TV band (that starts at 54 MHz, which corresponds to $z = 25$). This feature will appear as an about 100 mK “absorption line” in the spectrum of the Galactic foreground, and may be observable with future radio telescopes. The specific location of this feature is, of course, model dependent - a slight variation of cosmological parameters well within WMAP errors can either move it to higher redshifts, or hide it entirely behind the broadcast TV band. Thus in the later case, observing it will probably be impossible, but if indeed it falls beyond the broadcast TV band, it will clearly indicate the “first light” in the Universe - or, at least, first Lyman- α photons.

The observational situation with fluctuations is, in some sense, reversed with respect to the mean signal. While it will be significantly easier to separate fluctuations in redshifted 21 cm emission from the Galactic foreground, the early emission of Lyman- α photons relative to the growth of structure makes the fluctuation signal harder to observe than in more conventional reionisation models (Gnedin & Shaver 2003). In addition, at the predicted level of the cosmological signal, systematic errors such as beam leakage also become important. It, therefore, appears that unless the absorption feature at 54 MHz can be detected, existing and projected radio telescopes (including LOFAR and SKA) will not be able to detect cosmological fluctuations in the redshifted 21 cm signal in emission (but there still remain the possibility to detect the 21 cm forest in absorption against high redshift radio sources).

5 SECONDARY CMB ANISOTROPIES

Another possible observational signature of the early episode of X-ray emission is secondary CMB anisotropies. We used Gnedin & Jaffe (2001) method to compute the spectrum of secondary anisotropies on small angular scales (arcmin^2 or $l > 10^4$), where the anisotropies from the first episode of structure formation dominate other contributions. Maps of the temperature anisotropies for the X-ray preionisation simulation (run M-BH, left panel) and Population III stellar reionisation simulation (run 128L2VM in paper I, right panel) are shown in Fig. 12.

Fig. 12 shows the angular spectrum for runs M-BH and 128L2VM together with the typical spectrum from Gnedin & Jaffe (2001). A remarkable feature can be observed: while in a model without early episode of X-ray emission $C_l l(l+1)$ falls off at small angular scales approximately as $l^{-3/4}$, in our model

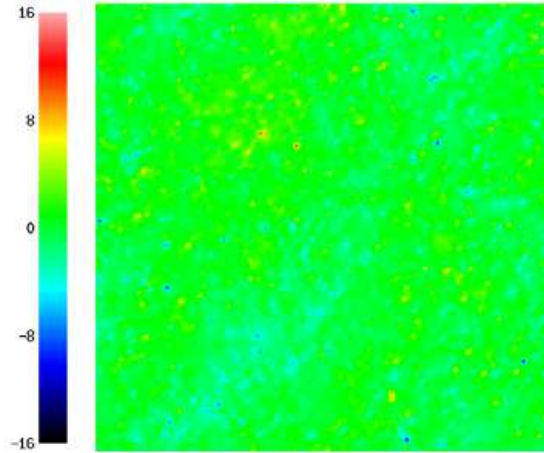


Figure 11. Secondary temperature anisotropies (in μK) in a 0.55×0.55 arcmin^2 patch of the sky for the run M-BH. The map shows strongly non-linear features produced by gas in minihaloes.

the anisotropies instead grow roughly as $l^{3/4}$. The temperature anisotropies are of the order of $\Delta T \sim 16 \mu\text{K}$ at ~ 1 arcsec scales. This opens up a unique opportunity to test our models against those without early episode of X-ray emission, although, observations on these scales are in the future and may be extremely difficult to separate the signal from the foreground sources contamination (but see, Fomalont et al. 1993; Church et al. 1997).

The non-linear Ostriker-Vishniac effect (Ostriker & Vishniac 1986) describes anisotropies generated in a universe in which the ionisation fraction is homogeneous in space. In our simulations the ionisation fraction is not homogeneous in space and the total power spectrum of the anisotropies includes a contribution from the “patchy reionisation”. In the X-ray preionisation model the non-linear OV component of the anisotropy power spectrum (calculated assuming the mean ionisation fraction) is actually slightly larger than the total signal, which means that the “patchy reionisation” component is mildly anti-correlated with the OV component. In other words, the higher density regions are less ionised than the low density regions - this is, obviously, a signature of X-ray ionisation. Such a separation is purely artificial and unphysical, but illustrates the main physical difference with the UV-ionisation models. Indeed, Gnedin & Jaffe (2001) have shown that in models in which reionisation is produced by UV from stellar sources the OV and “patchy reionisation” signals are instead strongly correlated.

The temperature anisotropies on these scales are dominated by non-linear structures and an analytical derivation is not possible. But it is clear from Fig. 12 that the early start of IGM ionisation in the X-ray models produces additional power on arcsec scales that should be roughly proportional to the mean fractional ionisation of the IGM during the extended period of X-ray pre-ionisation. In principle, the detection of anisotropies on these scales can be used to obtain precise measurements of the ionisation history of the IGM before the epoch of overlap when the reionisation is completed.

6 DISCUSSION AND SUMMARY

The present paper is the third in a series (see paper I and paper IIa) devoted to the study of physically plausible reionisation scenarios. The models have optical depths to Thompson scattering $\tau_e \sim 0.17$, as measured by WMAP (Kogut et al. 2003), and are consistent with

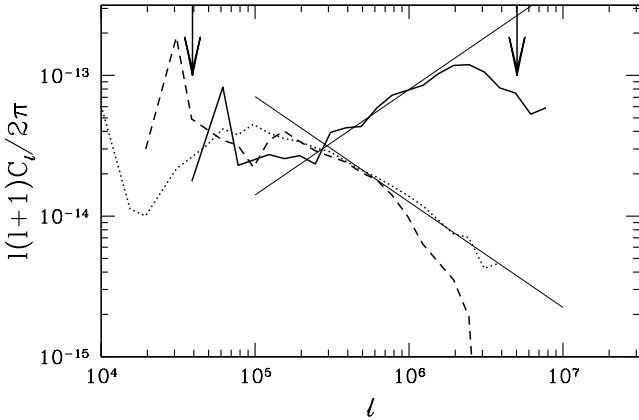


Figure 12. The power spectrum of the CMB anisotropies for the run **M-BH** (solid thick line). For comparison, the dashed and dotted lines show the power spectrum for two models without early X-ray sources: the dashed lines is the simulation **128L2noSN** with box size of $2 \text{ h}^{-1} \text{ Mpc}$ (from Ricotti & Ostriker 2003) and the dotted line is a simulation with box size of $4 \text{ h}^{-1} \text{ Mpc}$ (from Gnedin & Jaffe 2000). Two thin straight lines mark $+0.75$ and -0.75 slopes respectively. Two vertical arrows show the fundamental and the Nyquist frequencies of the simulated sky for the run **M-BH**.

observations of the IGM optical depth to Lyman- α and Lyman- β photons toward high redshift quasars (Fan et al. 2003; Songaila 2004). We have studied models of reionisation by stars (paper I) or mini-quasars (paper IIa) considering realistic physical scenarios and observational constraints. Our main conclusion is that it is very difficult for any of these models to produce optical depths in excess of 0.17. If this large optical depth is produced by ultraviolet radiation from stellar sources (*i.e.*, Population III stars with a top-heavy IMF), we find that zero-metallicity stars must be the dominant mode of star formation up to redshift $z \sim 10$. If this scenario is correct, we need to understand the reasons for the very inefficient mixing of metal enriched gas from SNe with the gas in which star formation takes place. At the moment this inefficient mixing is not reproduced by numerical simulations. A feasible alternative scenario requires that most Population III stars must implode into black holes without exploding as SNe or have subluminal SN explosions with a large amount of metal fall-back onto the compact remnant in order to reduce their metal yields. A scenario in which a large fraction of Population III stars end their lives as pair-instability supernovae is not compatible with the large optical depth to Thomson scattering measured by WMAP.

In this paper we use cosmological simulations to study a reionisation scenario in which standard reionisation by Population II stars is preceded by partial ionisation and reheating at early times by an X-ray background (*i.e.*, “X-ray preionisation” models studied in paper IIa using semianalytic simulations). In these models the ionisation rate from the secondary radiation produced by accretion on compact remnants from the first stars dominates over the primary ultraviolet radiation emitted by the stars during their lifetime. The most appealing aspect of these models is their insensitivity to the duration of the epoch of Population III stars domination. In fact, the relative importance of Population III stars with respect to Population II stars in practice has to be treated as a free parameter due to the large uncertainties in modelling the complex physical processes that regulate metal production and mixing.

In order to reproduce WMAP results we find that a fraction of about 10^{-4} of all the baryons in the Universe needs to

be accreted by compact objects before redshift 10. This fraction is comparable in mass to the observed mass density of supermassive BHs in the galactic nuclei today. This does not pose a strong constraint on the models because a sizeable fraction of these early intermediate-mass BHs is expected to be removed from the galaxies during the last phases of the merger or to reside in the interstellar medium of galaxies, being hardly detectable Madau & Rees (2001). Perhaps a small fraction of these intermediate-mass BHs may be accreting and contribute to the observed population of ULX (Agol & Kamionkowski 2002; Krolik 2004).

The stronger constraint on the model is posed by the observed soft X-ray background. Assuming that the early mini-quasars population produces an optical depth to Thomson scattering $\tau_e \sim 0.17$, their contribution to the background in the 5-50 keV bands is 5-20%. Future X-ray missions may be able to detect these sources if they exist. The predicted fluxes of the most rare objects is at the limit of the detection of the Chandra deep fields and about 1000 objects with flux $10^{-18} \text{ erg cm}^{-2} \text{ s}^{-1}$ should be present per 5.3 arcmin^2 . Note that these calculations assume a spectral energy distribution of the sources that has a non-negligible high energy power-law component (*cf.*, Fig. 4 in paper IIa), in agreement with observations of QSOs and ULX in the local universe. If the source spectra are dominated by a multicolour disk thermal component their contribution to both the X-ray background in the 2-50 keV bands and the faint source counts would be negligible.

The redshifted X-ray background also has interesting consequences for the reionisation history of He and the thermal history of the IGM at redshift $z \sim 3$, independently of the assumed spectra of the sources. In this paper we confirm the results of paper IIa in which we found that He II is almost fully reionised for the first time at redshift $z \sim 17$ and afterwards slowly recombines before experiencing a second reionisation at redshift $z \sim 3$ produced by the redshifted X-ray background. The heating rate from the background radiation keeps the temperature of the IGM at about 10,000 K, in rough agreement with observations of the line widths of the Lyman- α forest at $z \sim 3 - 4$. We also emphasise that the redshifted X-ray background is important in producing a fully ionised atomic hydrogen in the low density intergalactic medium before stellar reionisation at redshift $z \sim 6 - 7$. As a result stellar reionisation is characterised by an almost instantaneous “overlap phase” of H II regions.

The patchy topology of reionisation produced by stellar sources contrast with the spatially homogeneous partial ionisation by X-rays. This produces distinctive signatures on temperature/polarisation CMB anisotropies and on the redshifted 21cm emission/absorption from neutral hydrogen at high redshift.

(i) The power spectrum of the EE polarisation is sensitive to the visibility function $g(z)$, defined in equation (3). The Planck satellite should be able to distinguish between the visibility function produced by an early X-ray partial ionisation (*cf.*, Fig. 4 and Fig. 8 in paper IIa) or the one expected for reionisation by stellar sources (*cf.*, Fig. 4 in paper I).

(ii) On small angular scales ($< 1 \text{ arcmin}$ or $l > 10^4$) the secondary anisotropies produced by non-linear structures during the early reionisation epochs dominate over other contributions, offering a unique opportunity to study the first episode of structure formation. A remarkable feature can be observed: while in a model without early episode of X-ray emission the power spectrum falls off at small angular scales approximately as $l^{-3/4}$, in X-ray preionisation models the power instead grows roughly as $l^{3/4}$. The temperature anisotropies are of the order of $\Delta T \sim 16 \mu\text{K}$ at ~ 1

arcsec scales. But it is extremely difficult to detect anisotropies on these scales, partly because of foreground sources contamination (Fomalont et al. 1993; Church et al. 1997). In models in which reionisation is produced by UV from stellar sources the secondary anisotropies produced by the nonlinear Ostriker-Vishniac effect (*i.e.*, assuming uniform ionisation fraction) have less power than in the full calculation that includes the “patchy reionisation” signal (the signals are correlated). In X-ray preionisation models the nonlinear Ostriker-Vishniac effect and “patchy reionisation” signals are instead slightly anti-correlated.

(iii) The redshifted 21cm emission/absorption from neutral hydrogen is another powerful probe of the ionisation state of the IGM at high redshift. In X-ray preionisation models a sharp absorption feature at $z \sim 25 - 30$ falls just outside the broadcast TV bands. This feature will appear as a roughly 100 mK “absorption line” in the spectrum of the Galactic foreground, and may be observable with LOFAR. The partial ionisation of the IGM in the X-ray preionisation scenarios offers better opportunities to observe the fluctuations of the redshifted 21cm line in emission at redshifts lower than 10, where the signal is easier to measure.

Finally indirect signatures of X-ray preionisation are related to the discovery of massive BHs in the nuclei of dwarf galaxies and/or the identification of intermediate mass BHs in the ISM of galaxies (*e.g.*, ULX). If Population III stars are instead responsible for the large optical depth measured by WMAP future observations with JWST and ground based near-infrared Lyman- α surveys using gravitational lenses may soon be able to observe these objects (Pelló et al. 2004; Ricotti et al. 2004) and probe the ionisation state of the IGM.

ACKNOWLEDGEMENTS

MR is supported by a PPARC theory grant. NG was partially supported by NSF grant AST-0134373 and by National Computational Science Alliance under grant MCA03S023 and utilised IBM P690 array at the National Center for Supercomputing Applications. Research conducted in cooperation with Silicon Graphics/Cray Research utilising the Origin 3800 supercomputer (COSMOS) at DAMTP, Cambridge. COSMOS is a UK-CCC facility which is supported by HEFCE and PPARC. MR thanks Martin Haehnelt and the European Community Research and Training Network “The Physics of the Intergalactic Medium” for support. The authors would like to thank Andrea Ferrara, Martin Haehnelt, Piero Madau and Martin Rees for stimulating discussions.

REFERENCES

Agol, E., & Kamionkowski, M. 2002, MNRAS, 334, 553
 Alexander, D. M., et al. 2003, AJ, 126, 539
 Carilli, C. L., Gnedin, N. Y., & Owen, F. 2002, ApJ, 577, 22
 Cen, R. 2003a, ApJ, 591, L5
 Cen, R. 2003b, ApJ, 591, 12
 Chiu, W. A., Fan, X., & Ostriker, J. P. 2003, ApJ, 599, 759
 Church, S. E., Ganga, K. M., Ade, P. A. R., Holzapfel, W. L., Mayskopf, P. D., Wilbanks, T. M., & Lange, A. E. 1997, ApJ, 484, 523
 Ciardi, B., Ferrara, A., & White, S. D. M. 2003, MNRAS, 344, L7
 Comastri, A., Setti, G., Zamorani, G., & Hasinger, G. 1995, A&A, 296, 1

De Luca, A., & Molendi, S. 2004, A&A, 419, 837
 Dijkstra, M., Haiman, Z., & Loeb, A. 2004, ArXiv Astrophysics e-prints
 Fan, X., et al. 2003, AJ, 125, 1649
 Fomalont, E. B., Partridge, R. B., Lowenthal, J. D., & Windhorst, R. A. 1993, ApJ, 404, 8
 Gnedin, N. Y. 1995, ApJS, 97, 231
 Gnedin, N. Y. 1998, MNRAS, 294, 407
 Gnedin, N. Y., & Abel, T. 2001, New Astronomy, 6, 437
 Gnedin, N. Y., & Jaffe, A. H. 2001, ApJ, 551, 3
 Gnedin, N. Y., & Shaver, P. A. 2003, ArXiv Astrophysics e-prints
 Haiman, Z., Rees, M. J., & Loeb, A. 1997, ApJ, 476, 458
 Holder, G. P., Haiman, Z., Kaplinghat, M., & Knox, L. 2003, ApJ, 595, 13
 Hunt, M., Steidel, C., Adelberger, K., & Shapley, A. 2003, submitted (astro-ph/0312041)
 Koekemoer, A., et al. 2003, submitted (astro-ph/0306407)
 Kogut, A., et al. 2003, ApJS, 148, 161
 Krolik, J. H. 2004, ArXiv Astrophysics e-prints
 Machacek, M. E., Bryan, G. L., & Abel, T. 2003, MNRAS, 338, 273
 Madau, P., Meiksin, A., & Rees, M. J. 1997, ApJ, 475, 429
 Madau, P., & Rees, M. J. 2001, ApJ, 551, L27
 Madau, P., Rees, M. J., Volonteri, M., Haardt, F., & Oh, S. P. 2004, ApJ, 604, 484
 Miyaji, T., & Griffiths, R. E. 2002, ApJ, 564, L5
 Oh, S. P. 2001, ApJ, 553, 499
 Oh, S. P., & Mack, K. J. 2003, submitted (astro-ph/0302099)
 Ostriker, J. P., & Gnedin, N. Y. 1996, ApJ, 472, L63
 Ostriker, J. P., & Vishniac, E. T. 1986, ApJ, 306, L51
 Pelló, R., Schaerer, D., Richard, J., Borgne, J. L., & Kneib, J. 2004, A, 416, L35
 Ptak, A., Griffiths, R., White, N., & Ghosh, P. 2001, ApJ, 559, L91
 Ranalli, P., Comastri, A., & Setti, G. 2003, A&A, 399, 39
 Ricotti, M., Gnedin, N. Y., & Shull, J. M. 2000, ApJ, 534, 41
 Ricotti, M., Gnedin, N. Y., & Shull, J. M. 2001, ApJ, 560, 580
 Ricotti, M., Gnedin, N. Y., & Shull, J. M. 2002a, ApJ, 575, 33
 Ricotti, M., Gnedin, N. Y., & Shull, J. M. 2002b, ApJ, 575, 49
 Ricotti, M., Gnedin, N. Y., & Shull, J. M. 2004, in preparation
 Ricotti, M., Haehnelt, M. G., Pettini, M., & Rees, M. J. 2004, MNRAS, 352, L21
 Ricotti, M., & Ostriker, J. P. 2004a, MNRAS, 350, 539 (paper I)
 Ricotti, M., & Ostriker, J. P. 2004b, MNRAS, 352, 547
 Sazonov, S. Y., Ostriker, J. P., & Sunyaev, R. A. 2004, MNRAS, 347, 144
 Sokasian, A., Yoshida, N., Abel, T., Hernquist, L., & Springel, V. 2004, MNRAS, 350, 47
 Somerville, R. S., & Livio, M. 2003, ApJ, 593, 611
 Songaila, A. 2004, AJ, 127, 2598
 Spergel, D. N., et al. 2003, ApJS, 148, 175
 Tegmark, M., et al. 2004, Phys. Rev. D, 69, 103501
 Tozzi, P., Madau, P., Meiksin, A., & Rees, M. J. 2000, ApJ, 528, 597
 Umeda, H., & Nomoto, K. 2003, Nature, 422, 871
 Venkatesan, A., Giroux, M. L., & Shull, J. M. 2001, ApJ, 563, 1
 Whalen, D., Abel, T., & Norman, M. 2003, submitted (astro-ph/0310283)
 White, N. E., & Tananbaum, H. 1999, Astronomische Nachrichten, 320, 280
 Wyithe, J. S. B., & Loeb, A. 2003, ApJ, 588, L69